# Nonlinear effects in the ionospheric Alfvén resonator

D. Sydorenko,[1] R. Rankin,[1] and K. Kabin[1]

Received 3 July 2008; revised 12 August 2008; accepted 21 August 2008; published 15 October 2008.

[1] A two-dimensional nonlinear multi-fluid MHD model of the ionosperic Alfvén resonator is presented. The resonator is excited by a packet of shear Alfvén waves propagating downward toward the ionosphere from high altitudes. It is shown that the nonlinear (ponderomotive) force of standing oscillations in the ionospheric Alfvén resonator creates plasma flows along the geomagnetic field that modify the plasma density profile. Depending on the amplitude of the wave packet exciting the resonator, this effect can be very strong. For the selected plasma density profile in the near-Earth magnetosphere, an Alfvén wave packet with a smooth symmetric envelope and the maximum transverse electric field amplitude of 0.5 V/m, carrying 10 wave periods with the frequency of the first resonator harmonic, can decrease the plasma density by a factor of two at altitudes between 1000 and 1700 km in less than one minute. The amplitude of the wave packet is nonuniform in the direction across the geomagnetic field, which results in nonuniform density modification and phase mixing of oscillations on neighboring geomagnetic field lines. This increases both the transverse wavenumber of the excited resonator harmonics and the wave electric field along the geomagnetic field.

**Citation:** Sydorenko, D., R. Rankin, and K. Kabin (2008), Nonlinear effects in the ionospheric Alfvén resonator, *J. Geophys. Res.*, *113*, A10206, doi:10.1029/2008JA013579.

## 1. Introduction

[2] Large scale depletions (or cavities) of plasma density have been observed by satellites [*Persoon et al.*, 1988; *Lundin et al.*, 1994; *Chaston et al.*, 2007] and sounding rockets [*Boehm et al.*, 1990] at altitudes from several hundreds to several thousands kilometers. Most likely, these depletions occur due to diverging plasma flows. Although under certain conditions the density cavity may be caused by electron [*Bellan and Stasiewicz*, 1998] or ion [*Knudsen et al.*, 2004] displacement across the geomagnetic field, the plasma flows more easily along the geomagnetic field. Below, only the field-aligned plasma flows are considered as a possible reason for density cavity formation above the ionosphere.

[3] Density cavities are frequently accompanied by anisotropic ion heating [*Eriksson et al.*, 1994], which may increase the magnetic moment of ions and the associated mirror force leading to the ion outflow [*Singh*, 1994]. However, strong ion outflow events are not always correlated with ion heating, and thus, different acceleration mechanisms are possible [*Wahlund and Opgenoorth*, 1989; *Andre and Yau*, 1997]. In particular, ion flows can be produced by the ponderomotive force of electromagnetic waves propagating along the geomagnetic field [*Li and Temerin*, 1993; *Shukla et al.*, 1996].

[4] The ponderomotive force is a time-averaged nonlinear force, which defines slow-time-scale motion of a charged particle in spatially-nonuniform time varying electromagnetic fields [*Gaponov and Miller*, 1958; *Kentwell and Jones*, 1987]. It can be interpreted as wave pressure or as a momentum transfer from the wave to the medium. The ponderomotive force is responsible for density modification in laser plasmas [*Krushelnick et al.*, 1997], low-frequency inductive discharges [*Godyak et al.*, 2001], and many other phenomena. In the magnetosphere, the ponderomotive force associated with the so-called PC1 pulsations (electromagnetic ion-cyclotron waves with frequency in the range 0.2–5 Hz) may increase plasma density in the equatorial plane [*Guglielmi et al.*, 1993] or produce dense cold plasma clouds in the trough region [*Feygin et al.*, 1997].

[5] The simplest nonlinear force created by an electromagnetic wave in a plasma is the Lorentz force of the wave magnetic field acting on the wave current. The ponderomotive action of a shear Alfvén wave on ions is related to the transverse ion current and thus is directed along the geomagnetic field. Note, however, that the transverse electron displacement considered by *Bellan and Stasiewicz* [1998] occurs due to the ponderomotive force acting on electrons in the direction across the geomagnetic field, similar to the formation of plasma channel by an intense laser pulse [*Krushelnick et al.*, 1997].

[6] The ponderomotive force is proportional to the spatial gradient of the wave field amplitude. For travelling waves, the gradient is typically related to spatial decay or finite dimensions of the wave packet. For standing waves, the gradient appears naturally due to the presence of alternating nodes and antinodes of the field. Spatial structure of a standing wave in a resonator usually weakly changes with time. As a result, the ponderomotive force is applied for an extended time, which amplifies the ponderomotive effect in a resonator.

[1]Department of Physics, University of Alberta, Edmonton, Alberta, Canada.


0148-0227/08/2008JA013579

[7] There are two principal types of resonators for Alfvén waves in the magnetosphere. First is the global resonator bounded by the Northern and Southern ionospheres [e.g., *Cummings et al.*, 1969]. Second is the ionospheric Alfvén resonator (IAR) formed at high latitudes between the ionosphere and the Alfvén speed gradient at altitude of about 3–5 thousand kilometers [*Polyakov and Rapoport*, 1981]. It is known that the ponderomotive force of standing global Alfvénic oscillations can produce nonmonotonic plasma density distribution along the geomagnetic field [*Allan*, 1993]. The density decreases at points, in the neighborhood of which the ponderomotive force is directed away from the point. Such points are called "diverging nodes" by *Allan* [1993]. Note, however, that the length of the global resonator along the geomagnetic field is tens of thousands kilometers and a diverging node will appear at the altitude of about 1–2 thousand kilometers only if a resonator harmonic with frequency much larger than the fundamental resonator frequency is excited. Thus, it is unlikely that density cavities at such altitude can be formed due to the ponderomotive force of a global field line resonance. In contrast, the IAR is much shorter than the global Alfvén resonator, and the diverging nodes in the IAR may easily appear within the desired altitude range.

[8] The present paper describes a nonlinear two-dimensional (2D) MHD model of the IAR. Instead of using the approximate concept of the ponderomotive force, the self-consistent nonlinear force of the Alfvén wave is included in the model. Thus, only the term "nonlinear force" is used in the description of IAR simulations below. The 2D IAR simulations reveal that the nonlinear force of an intense standing shear Alfvén wave in the IAR may produce a deep density depression in less than one minute.

[9] Strong density modification significantly changes wave propagation. In this case, it is reasonable to expect additional nonlinear effects. For example, in case of oscillations driven by some external force, the density modification results in the growth of dephasing between the force and the oscillations and leads to the saturation of oscillations amplitude [*Rankin et al.*, 1994]. In the present 2D IAR model, the formation of a density cavity is accompanied by the increase of the transverse wavenumber and the wave electric field along the geomagnetic field, as explained below.

[10] In the cavity, the profile of the density in the direction across the geomagnetic field is formed by the wave nonlinear force and follows the profile of the intensity of the wave. Similar plasma density distribution also appears for global standing oscillations [*Guglielmi and Lundin*, 2001]. The nonuniform density depression leads to the gradient of the Alfvén speed across the ambient magnetic field. As a result, phase mixing of oscillations along neighboring magnetic field lines develops and leads to shorter transverse wavelengths.

[11] Phase mixing is well known in the physics of space plasmas. *Heyvaerts and Priest* [1983] in their studies of the solar corona heating consider phase mixing as the reason for different instabilities (e.g., the Kelvin-Helmholtz instability) and quick dissipation of the Alfvén wave energy. *Mann et al.* [1995] show that phase mixing combined with ionospheric dissipation limits the width of field line resonances. The reduction of wave transverse spatial scale in IAR due to phase mixing is discussed by *Lysak and Song* [2000] in case of prescribed nonuniformity of the plasma density. Two-dimensional kinetic simulations with periodic boundary conditions and prescribed initial nonuniform density profile (similar to the density cavity) show that saturation of the transverse wavenumber growth occurs when the transverse wavelength becomes comparable to the electron inertial length [*Genot et al.*, 2000, 2004]. This is accompanied by dissipation of the wave energy by the acceleration of electrons.

[12] Although both the nonuniform plasma density modification due to the nonuniform wave intensity profile [*Guglielmi and Lundin*, 2001] and phase mixing [*Heyvaerts and Priest*, 1983; *Mann et al.*, 1995; *Lysak and Song*, 2000; *Genot et al.*, 2000, 2004] are already known, the present 2D IAR model is the first to include both effects in a self-consistent manner.

[13] The paper is organized as follows. In section 2, the nonlinear force of the fundamental and the first harmonic of a one-dimensional Alfvén resonator with a step-wise profile of the Alfvén speed is obtained. In section 3, the formalism of the 2D IAR model is presented. Section 4 focuses on the final density profiles obtained in 2D IAR simulations with the fundamental and the first resonator harmonic. Section 5 describes transverse wavenumber dynamics in the IAR simulation with the first resonator harmonic. The validity of results obtained in sections 4 and 5, as well as approximations included in the model are discussed in section 6. Conclusions are given in section 7.

## 2. Nonlinear Force in a Simplified One-Dimensional Alfvén Resonator

[14] In the IAR, the Alfvén speed above the ionosphere grows smoothly with altitude (see the qualitative dash-dot curve in Figure 1). It is instructive to start with a simple one-dimensional (1D) model of such a resonator. Consider a half-space $x > 0$ bounded by a highly conductive media at $x = 0$, as shown in Figure 1. The half-space is filled with plasma and immersed in a uniform magnetic field $B_x < 0$. Assume that the plasma mass density $\rho(x)$ changes in a stepwise manner, so that for $x < 0 < H$ (region 1 in Figure 1) the Alfvén speed $V_A = |B_x|(\mu_0\rho)^{-1/2}$ is a constant $V_{A,1}$, and for $H < x$ (region 2 in Figure 1) the Alfvén speed is another constant $V_{A,2}$ (see the bold curve in Figure 1). Similar systems are often used for investigation of IAR properties[e.g., *Trakhtengerts et al.*, 2000; *Yeoman et al.*, 2008]. Below, the 1D model is used to provide expressions for the nonlinear force in the Alfvén resonator.

[15] Propagation of a plane Alfvén wave in the 1D resonator is described by the following system:

$$\frac{\partial E_y}{\partial x} = -\frac{\partial B_z}{\partial t}, \tag{1}$$

$$-\frac{\partial B_z}{\partial x} = \frac{1}{c^2}\frac{\partial E_y}{\partial t} + \mu_0 J_y, \tag{2}$$

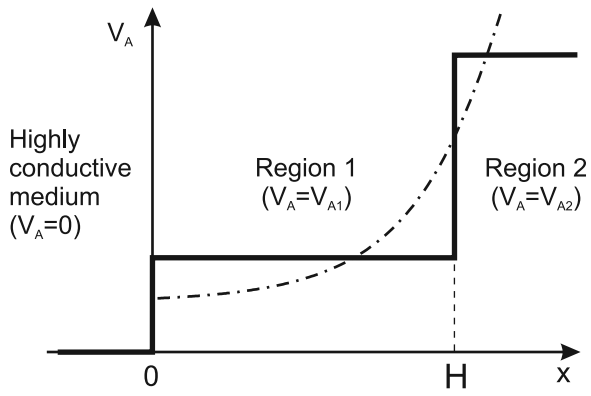


**Figure 1.** Alfvén speed profile (bold) in the 1D Alfvén resonator model. The dash-dot curve represents qualitatively the actual profile of Alfvén speed along a geomagnetic field line in the IAR.

where $E_y$ and $B_z$ are the wave field electric and magnetic components, respectively, $c$ is the light speed in free space, and the electric current $J_y$ is due to the ion inertia

$$J_y = \frac{1}{\mu_0 V_A^2}\frac{\partial E_y}{\partial t}. \tag{3}$$

[16] Assume that in region 1 the electromagnetic field is formed by two waves propagating along the $x$-axis in opposite directions, and in region 2 only a wave propagating in the positive $x$-direction exists. The electric field of these waves is taken in the form

$$\begin{aligned} E^{\pm}_{y,1}(x,t) &= A^{\pm}_1 \exp[\imath(\omega t \mp k_1 x)], \\ E^{+}_{y,2}(x,t) &= A^{+}_2 \exp[\imath(\omega t - k_2 x)], \end{aligned} \tag{4}$$

where superscripts + or − describe waves propagating in the positive and negative $x$-direction, subscripts 1 and 2 denote the regions, $\omega$ and $k$ are the wave angular frequency and wave number, $A^{\pm}_1$ and $A^{+}_2$ are the wave amplitudes. The boundary conditions are

$$\begin{aligned} E_{y,1}(0,t) = 0, E_{y,1}(H,t) &= E_{y,2}(H,t), \\ B_{z,1}(H,t) &= B_{z,2}(H,t), \end{aligned} \tag{5}$$

where $E_{y,1} \equiv E^{+}_{y,1} + E^{-}_{y,1}$, $E_{y,2} \equiv E^{+}_{y,2}$, $B_{z;1,2}$ is defined by (2) and (3) with $E_y = E_{y;1,2}$, respectively. Note, the condition at $x = 0$ corresponds to the boundary with infinite conductivity. Substituting (4) into (1) and (2) and applying (5) one obtains the following general expressions for the Alfvén wave magnetic field and current in region 1:

$$\begin{aligned} B_{z,1}(x,t) = \Re \sum_n \tilde{A}_{1,n}\frac{\tilde{k}_{1,n}}{\tilde{\omega}_n}\exp(\imath\tilde{\omega}_n t) \\ \times \left\{\exp\left(-\imath\tilde{k}_{1,n}x\right) - R\exp\left[\imath\tilde{k}_{1,n}(x-2H)\right]\right\}, \end{aligned} \tag{6}$$

$$\begin{aligned} J_{y,1}(x,t) = \Re \sum_n \tilde{A}_{1,n}\frac{\imath\tilde{\omega}_n}{\mu_0 V_{A,1}^2}\exp(\imath\tilde{\omega}_n t) \\ \times \left\{\exp\left(-\imath\tilde{k}_{1,n}x\right) + R\exp\left[\imath\tilde{k}_{1,n}(x-2H)\right]\right\}, \end{aligned} \tag{7}$$

where $\Re$ means the real part,

$$R = \frac{V_{A,eff,2} - V_{A,eff,1}}{V_{A,eff,2} + V_{A,eff,1}},$$

$R$ is the reflection coefficient,

$$\begin{aligned} \tilde{k}_{1,n} &= \frac{\pi}{H}\left(n + \frac{1}{2}\right) - \imath\frac{\ln|R|}{2H}, \\ \tilde{\omega}_{1,n} &= \tilde{k}_{1,n} V_{A,eff,1}, n = 0, 1, ..., \end{aligned}$$

$\tilde{k}_{1,n}$, $\tilde{\omega}_{1,n}$, and $\tilde{A}_{1,n}$ are the wave number, angular frequency, and amplitude of the resonator harmonic number $n$, $V^{-2}_{A,eff;1,2} = c^{-2} + V^{-2}_{A;1,2}$, and the tilde denotes a complex value. The nonlinear force acting on the plasma in the $x$-direction is the Lorentz force

$$F_{x,NL}(x,t) = J_y(x,t)B_z(x,t). \tag{8}$$

[17] Examples of profiles of the absolute value of the magnetic field (6), the absolute value of the electric current (7), and the nonlinear force (8) averaged over the wave period for the resonator harmonics $n = 0$ and $n = 1$ (referred to below as the fundamental and the first harmonics, respectively) are shown in Figure 2. Note, the nonlinear force for the fundamental harmonic (Figure 2c) does not change its sign within the resonator $0 < x < H$. Thus, there are no diverging nodes for the harmonic $n = 0$ inside the resonator. At the same time, the nonlinear force for the first harmonic (Figure 2f) changes its sign twice, forming a converging node at $x = H/3$ and a diverging node at $x = 2H/3$. The density will increase at the converging node and decrease at the diverging one. So, it is reasonable to expect

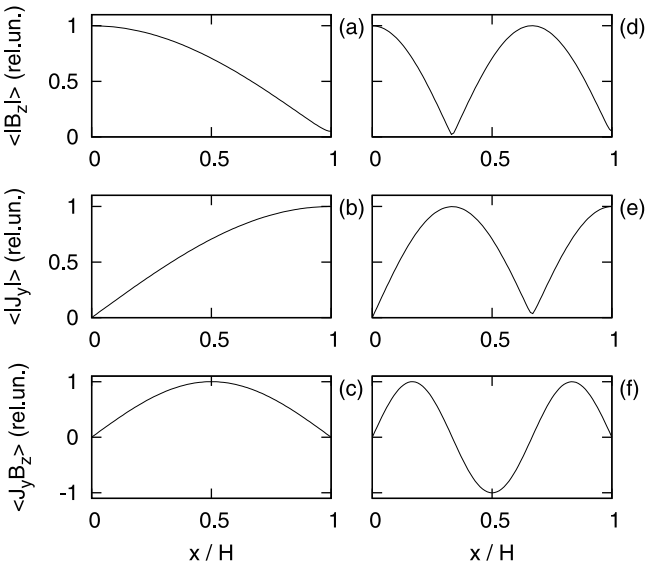


**Figure 2.** Profiles of the absolute value of magnetic field (a, d), the absolute value of electric current (b, e), and the nonlinear force (c, f). Panels (a), (b), and (c) are for the resonator harmonic $n = 0$. Panels (d), (e), and (f) are for the resonator harmonic $n = 1$. Profiles are averaged over the period $T_n = 2\pi/\Re\tilde{\omega}_n$ of the corresponding harmonic.

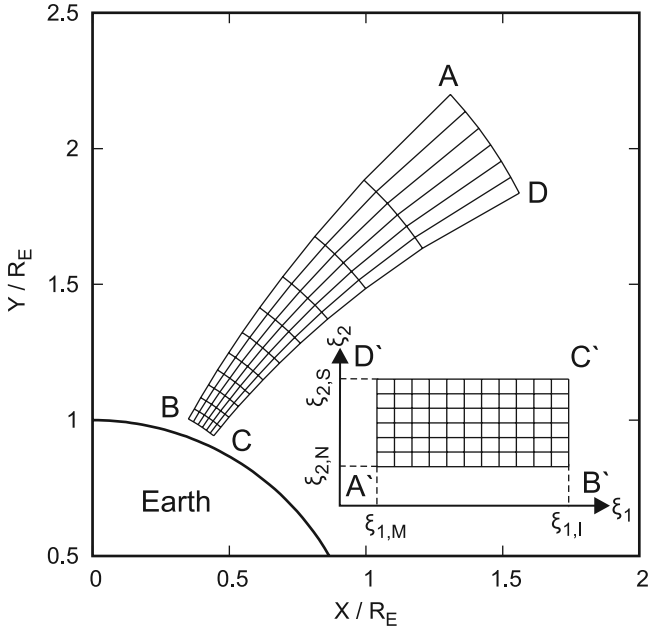


**Figure 3.** Schematic of the simulated area. Corners $A$, $B$, $C$, $D$ of the area in the real configuration space correspond to the corners $A'$, $B'$, $C'$, $D'$ of the rectangle in the dipole coordinate space, respectively.

that if the harmonic $n = 1$ is excited in the IAR with upper boundary at altitude of about 3000 km, the density depression due to the nonlinear force will occur at altitude of about 2000 km, which is consistent with satellite observations.

[18] Note, higher resonator harmonics ($n = 2,3,\ldots$) will produce additional diverging and converging nodes, with stronger nonlinear force due to the larger field gradients. However, aside from the stronger nonlinear force there will be no qualitative difference from the case $n = 1$, which is why below the IAR simulations are represented for the fundamental and the first IAR harmonics only.

## 3. Two-Dimensional Model of the Ionospheric Alfvén Resonator

[19] A two-dimensional IAR model is used to study propagation of a low-frequency inertial Alfvén wave along the geomagnetic field in the strongly non-uniform near-Earth plasma in the Northern hemisphere. The geomagnetic field is taken to be dipole. The model uses dipole coordinates $\xi_1 = \cos\vartheta/r^2$, $\xi_2 = \sin^2\vartheta/r$, and $\xi_3 = -\varphi$, where $\{r, \vartheta, \varphi\}$ are the ordinary spherical coordinates. The model resolves $\xi_1$ and $\xi_2$ coordinates, wave and plasma parameters do not depend on $\xi_3$ (i.e., the azimuthal symmetry is assumed). A typical area considered by the model is shown schematically in Figure 3. It is a curvilinear shape $ABCD$ in the configuration space, which corresponds to a rectangle $A'B'C'D'$ in the dipole coordinate space, with $\xi_{1,M} < \xi_1 < \xi_{1,I}$ and $\xi_{2,N} < \xi_2 < \xi_{2,S}$, where subscripts $M$, $I$, $N$, $S$ stand for "magnetosphere", "ionosphere", "North", and "South", respectively. Segment $BC$ approximates the top-layer of the ionosphere. In the present paper, the conductivity of this boundary is infinite.

[20] The plasma consists of cold electrons, hydrogen ions and oxygen ions. It is assumed that the plasma stays quasineutral all the time. Initial oxygen ($n_O$) and hydrogen ($n_H$) ion densities are

$$n_O(r)|_{t=0} = n_O^0 \exp\left(-\frac{r - R_E - h_I}{l_O}\right),$$
$$n_H(r)|_{t=0} = n_H^0 \left(\frac{R_E + h_I}{r}\right)^p, \tag{9}$$

where $n_O^0 = 10^{11}$ m$^{-3}$, $n_H^0 = 2 \times 10^7$ m$^{-3}$, $R_E = 6380$ km is the Earth radius, $h_I = 400$ km is the altitude of the top ionospheric layer, $l_O$ is the spatial scale of the oxygen ion density decay, $p = 1$ [*Lysak*, 2004]. Ion density profiles along the geomagnetic field line at the middle of the considered area are shown in Figure 4a. In this figure, the densities are plotted as functions of the distance from the ionospheric boundary $L_1$ calculated as

$$L_1(\xi_1, \xi_2) = \int_{\xi_1}^{\xi_{1,I}} d\xi_1' h_1(\xi_1', \xi_2)$$

where $h_1$ is the metric factor defined below, $\{\xi_1, \xi_2\}$ are the dipole coordinates of the observation point [$\xi_2$ is typically selected at the middle of the simulated area, $\xi_2 = (\xi_{2,N} + \xi_{2,S})/2$], and $\xi_{1,I}$ is the first dipole coordinate of the ionospheric boundary (segment $BC$ in Figure 3). Note, all profiles along the middle geomagnetic field line shown in the present paper are obtained in the same way. Profiles of the Earth magnetic field and the effective Alfvén speed $V_{A,eff} \equiv [c^{-2} + \mu_0(m_O n_O + m_H n_H)/B_E^2]^{-1/2}$, where $m_O$ and $m_H$ are the oxygen and hydrogen ion masses, are given in Figures 4b and 4c, respectively. The maximum gradient of $V_{A,eff}$ is at $L_1 \approx$

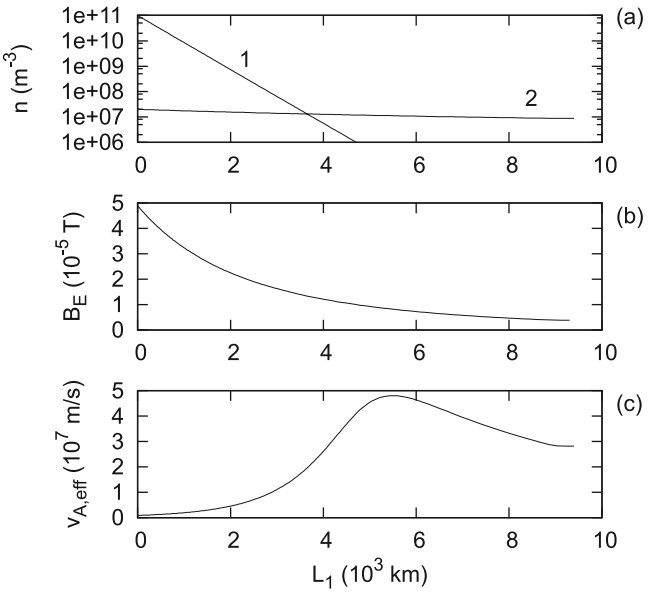


**Figure 4.** Profiles of oxygen (curve 1) and hydrogen (curve 2) ion number densities (a), Earth magnetic field (b), and effective Alfvén velocity (c) along the middle geomagnetic field line. $L_1 = 0$ at the ionospheric boundary.

4000 km, which is the high-altitude boundary of the IAR for the selected parameters.

[21] The following assumptions are made. First, it is assumed that the wave has a linear polarization with three field components $E_1$, $E_2$, and $B_3$. Second, cyclotron rotation is omitted, motion of all plasma components in the azimuthal $\xi_3$-direction is the drift in the crossed geomagnetic field and the transverse wave electric field $E_2$. Since the $E \times B$ drift velocity does not depend on the mass of the drifting particle, there is no electric current in the $\xi_3$-direction. Third, all plasma components are cold – there is no plasma pressure and mirror force. Fourth, the nonlinear convective term $(\mathbf{v} \cdot \nabla)\mathbf{v}$, which produces the centrifugal force in curvilinear coordinates, and the gravity force are omitted. Fifth, electrons move along the geomagnetic field (in the $\xi_1$-direction) due to the wave electric field $E_1$ but do not move across the geomagnetic field in the $\xi_2$-direction, while the ions can move both along the $\xi_1$ and $\xi_2$-directions. The above assumptions restrict the model capabilities, however, they are reasonable for description of Alfvén waves with frequency well below the cyclotron frequencies of ion species. The simplifications of the plasma dynamics restrict the applicability of the model to the low-altitude regions, where the geomagnetic field is strong and the plasma temperature is low. These conditions are satisfied within the IAR. Further discussion of the model applicability is given in section 6.

[22] The model uses Maxwell's equations

$$\frac{\partial E_1}{\partial t} = \frac{c^2}{h_2 h_3}\frac{\partial (h_3 B_3)}{\partial \xi_2} - c^2 \mu_0 e\left(\sum_{\alpha=O,H} n_\alpha v_{\alpha,1} - n_e v_{e,1}\right), \quad (10)$$

$$\frac{\partial E_2}{\partial t} = -\frac{c^2}{h_1 h_3}\frac{\partial (h_3 B_3)}{\partial \xi_1} - c^2 \mu_0 e \sum_{\alpha=O,H} n_\alpha v_{\alpha,2}, \quad (11)$$

$$\frac{\partial B_3}{\partial t} = -\frac{1}{h_1 h_2}\left[\frac{\partial (h_2 E_2)}{\partial \xi_1} - \frac{\partial (h_1 E_1)}{\partial \xi_2}\right], \quad (12)$$

combined with equations of motion for electrons and ions

$$\frac{\partial v_{e,1}}{\partial t} = -\frac{e}{m_e} E_1, \quad (13)$$

$$\frac{\partial v_{\alpha,1}}{\partial t} = \frac{e}{m_\alpha}\left(E_1 + v_{\alpha,2} B_3\right), \alpha = O, H, \quad (14)$$

$$v_{\alpha,2} = \frac{m_\alpha}{e B_E^2}\frac{\partial E_2}{\partial t}, v_{\alpha,3} = -\frac{E_2}{B_E}, \alpha = O, H, \quad (15)$$

the condition of quasineutrality

$$n_e = n_O + n_H,$$

and the continuity equations for ions

$$-\frac{\partial n_\alpha}{\partial t} = \frac{1}{h_1 h_2 h_3}\left[\frac{\partial \left(n_\alpha v_{\alpha,1} h_2 h_3\right)}{\partial \xi_1} + \frac{\partial \left(n_\alpha v_{\alpha,2} h_1 h_3\right)}{\partial \xi_2}\right], \alpha = O, H, \quad (16)$$

where subscripts 1, 2, 3 refer to components in the directions of $\xi_{1,2,3}$, respectively, $h_{1,2,3}$ are the metric factors, $h_2 = r^2/(\sin\vartheta\sqrt{1+3\cos^2\vartheta})$, $h_3 = r\sin\vartheta$, $h_1 = h_2 h_3$, $e > 0$ is the elementary charge, $m_e$, $n_e$, and $v_{e,1}$ are the electron mass, density, and velocity, $m_\alpha$, $n_\alpha$, and $v_{\alpha,1,2,3}$ are the mass, density, and velocity components of hydrogen ions (subscript $\alpha = H$) and oxygen ions (subscript $\alpha = O$), $B_E$ is the geomagnetic field (in the positive $\xi_1$-direction).

[23] The wave properties of the above system can be studied by substituting an electromagnetic wave with components

$$E_{1,2}(\xi_1, \xi_2, t) = \frac{E^a_{1,2}}{h_{1,2}}\exp(\imath\phi),$$
$$B_3(\xi_1, \xi_2, t) = \frac{B^a_3}{h_3}\exp(\imath\phi),$$

where $E^a_{1,2}$ and $B^a_3$ are constants, $\phi \equiv \omega t - \int d\xi_1 k_1 h_1 - \int d\xi_2 k_2 h_2$ is the wave phase, $\omega$ is the wave angular frequency, and $k_{1,2}$ are the wave number vector components, into Maxwell's equations (10)–(12). The electric currents can be calculated using the equations of motion (13)–(15) with the nonlinear terms omitted and the electron and ion densities constant. The resulting dispersion equation is

$$\omega^2 = \frac{k_1^2 V_{A,eff}^2\left(1 - \omega^2\lambda_e^2/c^2\right)}{1 + k_2^2\lambda_e^2 - \omega^2\lambda_e^2/c^2}, \quad (17)$$

where $\lambda_e = c/\omega_{pe}$ is the electron inertial length, $\omega_{pe} = [n_e e^2/(\varepsilon_0 m_e)]^{1/2}$ is the electron plasma frequency. Equation (17) has two independent roots. One root gives the high frequency oscillations $\omega \approx \omega_{pe}$, which is of no interest for the present study. The other root at low frequencies $\omega \ll \omega_{pe}$ is $\omega \approx k_1 V_{A,eff}/(1 + k_2^2\lambda_e^2)^{1/2}$, which corresponds to the inertial Alfvén wave.

[24] The IAR is excited by an Alfvén wave packet injected from the high altitude boundary (segment $AD$ in Figure 3). In order to combine wave injection with nonreflecting propagation of the outgoing wave, the equations for the Alfvén wave characteristics $F^\pm$ propagating in the positive (+ superscript) and negative (− superscript) $\xi_1$-directions are derived from Maxwell's equations (11) and (12):

$$\frac{\partial F^\pm}{\partial t} \pm \frac{V_{A,eff}}{h_1}\frac{\partial F^\pm}{\partial \xi_1} = 0, \quad (18)$$

where $F^\pm \equiv h_2(E_2 \pm V_{A,eff} B_3)$. The boundary condition at the high altitude boundary, first, calculates the incoming wave characteristic $F^+$ as some user-defined function of transverse coordinate $\xi_2$ and time $t$, and, second, uses equation (18) with the minus sign to find the outgoing characteristic $F^-$.

[25] Equations (18) are obtained using the method described in [*LeVeque*, 1992]. These equations are approximate and are obtained omitting the wave electric field $E_1$ and assuming that the metric factors and the Alfvén speed change on spatial scales much larger than the wavelength.

[26] The boundary condition at the ionospheric boundary with infinite conductivity (segment $BC$ in Figure 3) is

$$E_2\left(\xi_{1,J}\right) = 0.$$

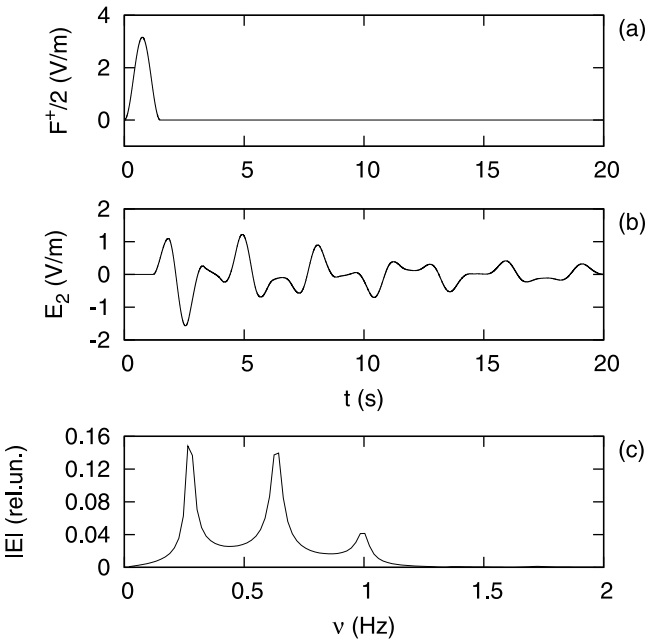


**Figure 5.** Linear simulation with plasma density held constant in time. (a) Electric field $E_2$ of the incoming Alfvén pulse versus time at the middle of the magnetospheric boundary. (b) Temporal evolution of the electric field of oscillations excited in the IAR at the point on the middle geomagnetic field line at $L_1 = 308$ km from the ionospheric boundary. (c) Spectrum of the frequency of the signal shown in (b).

The boundary condition at the boundaries coinciding with geomagnetic field lines (segments *AB* and *DC* in Figure 3) is

$$\left.\frac{\partial h_3 B_3}{\partial \xi_2}\right|_{\xi_2=\xi_{2;S,N}} = 0.$$

The latter condition corresponds to the assumption that along these boundaries a purely transverse Alfvén wave propagates, with $k_2 = 0$ and $E_1 = 0$.

## 4. Modification of the Plasma Density by the Nonlinear Force

[27] The area for the IAR simulation described in the present paper is selected as follows. The Southern ionospheric corner (*C* in Figure 3) is at the latitude 69.68° and altitude 400 km [same as $h_I$ in the equations for the ion density profiles (9)], which allows to define $\xi_{1,I}$ and $\xi_{2,S}$. The Northern ionospheric corner (*B* in Figure 3) is at latitude 70°, which defines $\xi_{2,N}$. Finally, the South magnetospheric corner (*D* in Figure 3) is at latitude 58°, which gives $\xi_{1,M}$. For the parameters above, the width of the ionospheric boundary (segment *BC* in Figure 3) is 38.3 km, the width of the magnetospheric boundary (segment *AD* in Figure 3) is 149.5 km, the distance between the midpoints of these boundaries calculated along the geomagnetic field line is 9400 km. Note, the actual area is much more narrow than the one shown in Figure 3. The computational grid has 200 cells in the $\xi_1$-direction and 100 cells in the $\xi_2$-direction.

[28] The incoming wave characteristic is defined as the following function of coordinate and time:

$$F^+(\xi_2,t) = 2E_2^+ \sin^2\left(\pi\frac{\xi_2-\xi_{2,\min}}{\xi_{2,\max}-\xi_{2,\min}}\right)\times\sin^2\left(\pi\frac{t}{T_{env}}\right) \times \sin(\omega t)\Pi(\xi_2,t), \quad (19)$$

where $E_2^+$ is the amplitude of the electric field of the incoming Alfvén wave, $\xi_{2,\min} = \xi_{2,N} + 0.1(\xi_{2,S} - \xi_{2,N})$ and $\xi_{2,\max} = \xi_{2,N} + 0.9(\xi_{2,S} - \xi_{2,N})$ are the transverse boundaries of the incoming wave, $\omega$ is the wave frequency, $T_{env}$ is the duration of the wave packet envelope, $\Pi(\xi_2,t) = 1$ if both $0 < t < T_{env}$ and $\xi_{2,\min} < \xi_2 < \xi_{2,\max}$, otherwise $\Pi(\xi_2, t) = 0$.

[29] Following section 1, two cases are considered, in which either the fundamental or the first IAR harmonic is excited. The eigenfrequencies of the IAR are defined in a linear test simulation, where the electron and ion densities remain constant in time and the ion motion along the geomagnetic field is due to the wave electric field $E_1$ only. In the linear simulation, the IAR is excited by a solitary unipolar pulse produced by equation (19) with $E^+ = 3.16$ V/m, $\omega = 0$, $T_{env} = 1.5$ s. The incoming pulse is shown in Figure 5a, the oscillations excited in the IAR are shown in Figure 5b, and the frequency spectrum of the IAR oscillations is shown in Figure 5c. The spectrum provides the frequency of the fundamental IAR harmonic $\nu_0 = 0.274$ Hz and that of the first harmonic $\nu_1 = 0.635$ Hz.

[30] In the nonlinear simulation with the fundamental IAR harmonic, parameters of the incoming wave (19) are $E_2^+ = 0.5$ V/m, $\omega = 2\pi\nu_0 = 1.72$ s$^{-1}$, and $T_{env} = 6/\nu_0 = 21.9$ s. These parameters produce a wave packet with smooth envelope containing 6 wave periods with frequency of the fundamental IAR harmonic (see Figure 6a). Note, the transverse ion velocity (15) and the nonlinear force in (14) are proportional to the ion mass, which is why it is convenient to characterize the nonlinear force by the acceleration which is the same for both ion species:

$$a_{1,NL} = \frac{e}{m_\alpha} v_{\alpha,2} B_3 = \frac{B_3}{B_E^2}\frac{\partial E_2}{\partial t}. \quad (20)$$

Profile of the nonlinear acceleration averaged over the fundamental harmonic period and profile of the ion velocity along the geomagnetic field are given in Figures 6b and 6c, respectively. Similar to the 1D Alfvén resonator (Figure 2c), the nonlinear force does not change its sign within the IAR (up to the altitudes of about 3000 km) and the plasma is accelerated upward (away from the ionosphere). Note, since $\xi_1$ increases *towards* the Earth while $L_1$ increases *away* from the Earth, the profile of $-v_1(L_1)$ is shown in Figure 6c in order to be consistent with the 1D resonator model and Figure 2 in the following: the positive force (acceleration) and the positive plasma flow are directed away from the highly conductive boundary (i.e., the ionosphere). At altitudes below 3–4 thousand km, the profiles $\langle -a_{1,NL}\rangle(L_1)$, where $\langle\ldots\rangle$ denotes averaging over the wave period, and $-v_1(L_1)$ for oxygen and hydrogen ions are virtually indistinguishable, which is why in Figures 6b and 6c only the oxygen profiles are shown. The same holds for Figure 7.

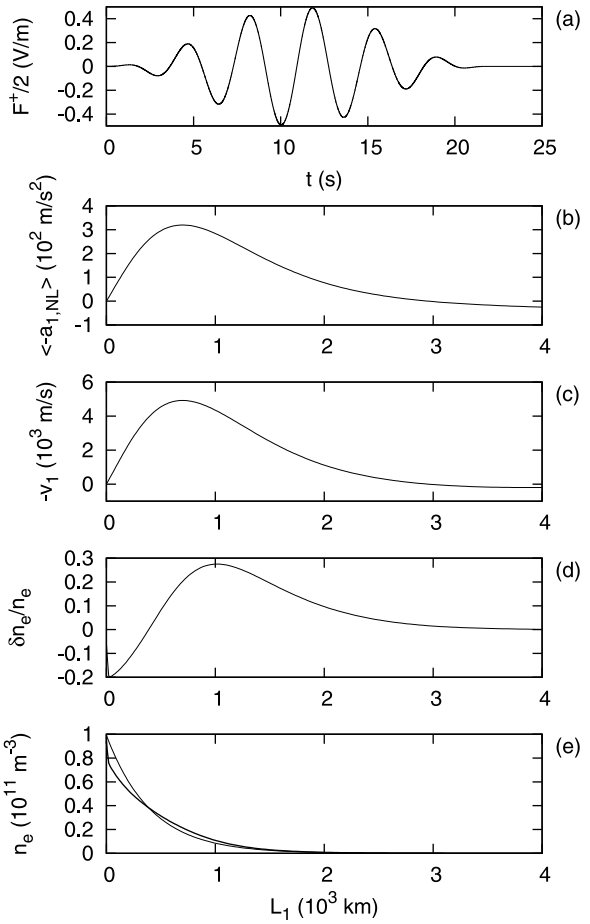


**Figure 6.** Nonlinear simulation with the fundamental IAR harmonic. (a) Electric field of the incoming wave versus time at the middle of the magnetospheric boundary. (b–e) Profiles of average acceleration due to the nonlinear force taken with the "minus" sign (b), ion velocity along the geomagnetic field taken with the "minus" sign (c), relative plasma density perturbation (d), and plasma density (e). Positive values in (b) and (c) are directed upward, away from the ionosphere $L_1 = 0$. Averaging in (b) is performed over one wave period starting at $t = 15.8$ s. Ion velocity in (c), relative density perturbation in (d), and the density profile shown by the bold curve in (e) are obtained at $t = 40$ s. Thin curve in (e) is the initial plasma density profile. The relative density perturbation in (d) is calculated as $n_e(t)/n_e(0) - 1$, where $n_e(t)$ is the plasma density at time $t$ and $n_e(0)$ is the initial plasma density.

[31] Density modification is defined by the continuity equation (16). With time, the first term in the right hand side of (16) becomes dominant, because the average contribution of the second term approaches zero due to the oscillating behavior of $v_{\alpha,2}$. It is instructive to consider equation (16) without the term proportional to $v_{\alpha,2}$, as follows

$$\frac{\partial n_\alpha}{\partial t} \approx -\frac{v_{\alpha,1}}{h_1}\frac{\partial n_\alpha}{\partial \xi_1} - \frac{n_\alpha}{h_1 h_2 h_3}\frac{\partial v_{\alpha,1} h_2 h_3}{\partial \xi_1}. \quad (21)$$

In a sizeable fraction of the IAR, the sign of the density modification is defined by the large density gradient in the first term in the right hand side of (21). Since the density gradient is directed downward and the field aligned ion flow is directed upward, this term is positive and the plasma density increases (see Figure 6d for $L_1 > 350$ km). However, there is a node of ion velocity $v_{\alpha,1}$ at the ionospheric boundary (see Figure 6c at $L_1 = 0$). At this node, the first term in the right-hand side of (21) vanishes, while the second term is negative because $h_{2,3} \approx const$ and $\partial v_{\alpha,1}/\partial \xi_1 > 0$. The result is the decrease of the plasma density in the immediate vicinity of the ionospheric boundary (see Figure 6d for $0 < L_1 < 350$ km).

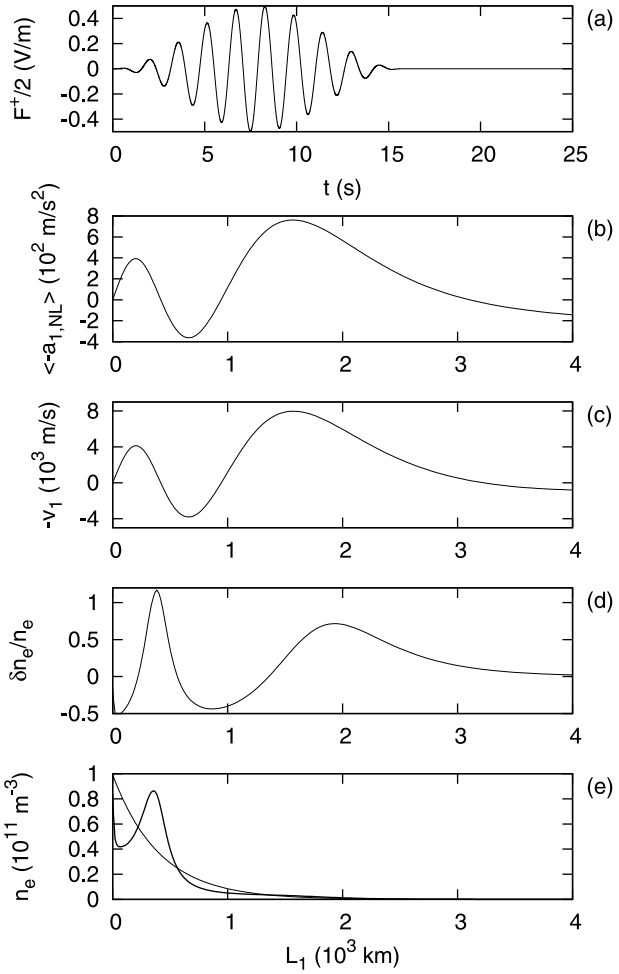


**Figure 7.** Nonlinear simulation with the first IAR harmonic. (a) Electric field of the incoming wave versus time in the midddle of the magnetospheric boundary. (b–e) Profiles of average acceleration due to the nonlinear force taken with the "minus" sign (b), ion velocity along the geomagnetic field taken with the "minus" sign (c), relative plasma density perturbation (d), and plasma density (e). Positive values in (b) and (c) are directed upward, away from the ionosphere $L_1 = 0$. Averaging in (b) is performed over the wave period starting at $t = 12.5$ s. Ion velocity in (c), relative density perturbation in (d), and the density profile shown by the bold curve in (e) are obtained at $t = 40$ s. Thin curve in (e) is the initial plasma density profile. The relative density perturbation in (d) is calculated as $n_e(t)/n_e(0) - 1$, where $n_e(t)$ is the plasma density at time $t$ and $n_e(0)$ is the initial plasma density.

[32] Density modification immediately near the ionosphere largely depends on the ionospheric boundary condition. If the ionosphere is highly conductive, as it is assumed in the present paper, the transverse electric field of the Alfvén wave at this boundary is zero, which results in the zero transverse ion flow and zero nonlinear force. If the ionospheric conductivity is finite, both the transverse electric field and transverse ion flow will be nonzero, the nonlinear force will accelerate the plasma at the boundary, which will remove the node for $v_{\alpha,1}$ at $L_1 = 0$ and increase the role of the density gradient term in (21). Thus, if the ionosphere has finite conductivity, the plasma density near the ionosphere may increase as well as in the other part of the IAR. Studies with the finite conductivity boundary are left for future work and are out of the scope of the present paper.

[33] The nonlinear simulation with the fundamental IAR harmonic reveals no density depression at the desired range of altitude [1000–2000 km, compare the final (bold curve) and the initial (thin curve) density profiles in Figure 6e]. A simulation in which the first IAR harmonic is excited is carried out with $E_2^+ = 0.5$ V/m, $\omega = 2\pi\nu_1 = 3.99$ s$^{-1}$, and $T_{env} = 10/\nu_1 = 15.75$ s. The incoming wave packet is shown in Figure 7a. This simulation reveals additional features of the plasma dynamics in the IAR. First, a strong density depression forms immediately near the ionospheric boundary due to the velocity node at this point, similar to the depression in the simulation with the fundamental IAR harmonic described above. Second, the nonlinear force changes its sign within the IAR twice with altitude (Figure 7b), similar to the 1D Alfvén resonator (Figure 2f). As a result, the ion velocity profile (Figure 7c) has a converging point at $L_1 \approx 450$ km and a diverging point at $L_1 \approx 950$ km. By the end of the simulation, the plasma density increases around the converging point and decreases around the diverging point (Figure 7d). A significant density depression with maximum amplitude of about 45% of the background density is formed between $L_1 = 550$ km and $L_1 = 1350$ km within 40 seconds after the beginning of the simulation [see Figure 7d and, also, compare the initial density profile (thin curve) with the final density profile (bold curve) in Figure 7e]. Note, although the incoming wave is rather intense, Alfvén waves with amplitudes of about 0.5–1 V/m were identified in space [*Chaston et al.*, 2002] and thus may contribute to the formation of density depressions at altitudes about 1–2 thousand kilometers.

## 5. Phase Mixing

[34] Modification of the plasma density due to the nonlinear force is proportional to the wave intensity and is nonuniform in the $\xi_2$ direction (across the geomagnetic field). The nonuniform density profile results in the phase mixing of oscillations along neighbor field lines and in appearance of large transverse wavenumbers $k_2$. As an example, consider the simulation with the first IAR harmonic described above. Figure 8 presents temporal dependences obtained at a point located on the middle field line inside the IAR, at a distance of $L_1 = 652$ km from the ionospheric boundary. This point is close to the minimum of the density depression shown in Figure 7d. As the simulation progresses, the amplitude of IAR oscillations grows while the IAR oscillations are driven by the incoming wave packet (see Figure 8a for $0 < t < 12$ s). Then, the growth changes to exponential decay as the wave energy leaks out of the resonator through the semi-transparent Alfvén-speed-gradient boundary. The nonlinear force rises and decays faster than the wave field amplitude because it is proportional to the squared wave field (see Figure 8b). The maximum nonlinear force is registered at the same time as the maximum of the IAR oscillations intensity, about $t \approx 12$ s. Plasma is virtually immobile for $t < 5$ s, then it undergoes intense acceleration during a short time interval $8\text{ s} < t < 18$ s, and afterwards the plasma keeps its velocity approximately constant due to its inertia (see Figure 8c). The plasma density depends, via the continuity equation (16), on the plasma speed and on the time interval the plasma flow exists. The density perturbation becomes noticeable at $t \approx 10–12$ s, when the plasma receives a significant push from the nonlinear force, and it continues to grow with time afterwards (see Figure 8d).

[35] In Figure 9, the transverse profiles of the plasma density and the wave field are presented for three consecutive times $t_{1,2,3}$ marked by vertical lines 1, 2, and 3 in Figure 8a. Each of these profiles is a function of distance $L_2$ from the Northern geomagnetic field line boundary (segment *AB* in Figure 3) along the line $\xi_1 = const$ defined as follows:

$$L_2(\xi_1, \xi_2) = \int_{\xi_{2,N}}^{\xi_2} d\xi_2' h_2(\xi_1, \xi_2').$$

Deformation of the density profile due to the nonlinear force is barely visible at time $t_1$ (curve 1 in Figure 9a), noticeable at time $t_2$ (curve 2 in Figure 9a), and large at time $t_3$ (curve 3 in Figure 9a). The evolution of the wave field towards shorter transverse wavelengths is shown in Figure 9b for the magnetic field $B_3$ and in Figure 9c for the electric field $E_1$. The $B_3$ profiles gradually decay. At the same time, the amplitude of the $E_1$ profiles grows with time. For comparison, temporal dependences $E_1(t)$ obtained in nonlinear and linear simulations with the same initial conditions and incoming wave parameters are given in Figures 8e and 8f, respectively. In the linear simulation, the density remains constant in time, the large transverse wavenumbers do not appear, and $E_1$ decays similar to $B_3$ (compare Figure 8f with Figure 8a). In the nonlinear simulation, the behavior of the $E_1$ amplitude is quite different from $B_3$ (compare Figure 8e with Figure 8a).

[36] Despite the amplification caused by the transverse wavenumber growth, the electric field $E_1$ of the inertial Alfvén wave in the IAR region stays very small ($E_1 < 10^{-7}$ V/m, the wave electric field $E_1$ in Figure 8e is even smaller because it is obtained in the midplane, where $E_1$-amplitude has a minimum). Although electron acceleration in the magnetosphere is out of the scope of the present paper, it is necessary to mention that such weak fields cannot produce significant particle acceleration inside the IAR area. This suggests that other processes not included in the model are important. In particular, possibilities include nonlocal kinetic effects [*Rankin et al.*, 1999; *Watt et al.*, 2004; *Lysak and Song*, 2005], anomalous plasma resistivity and

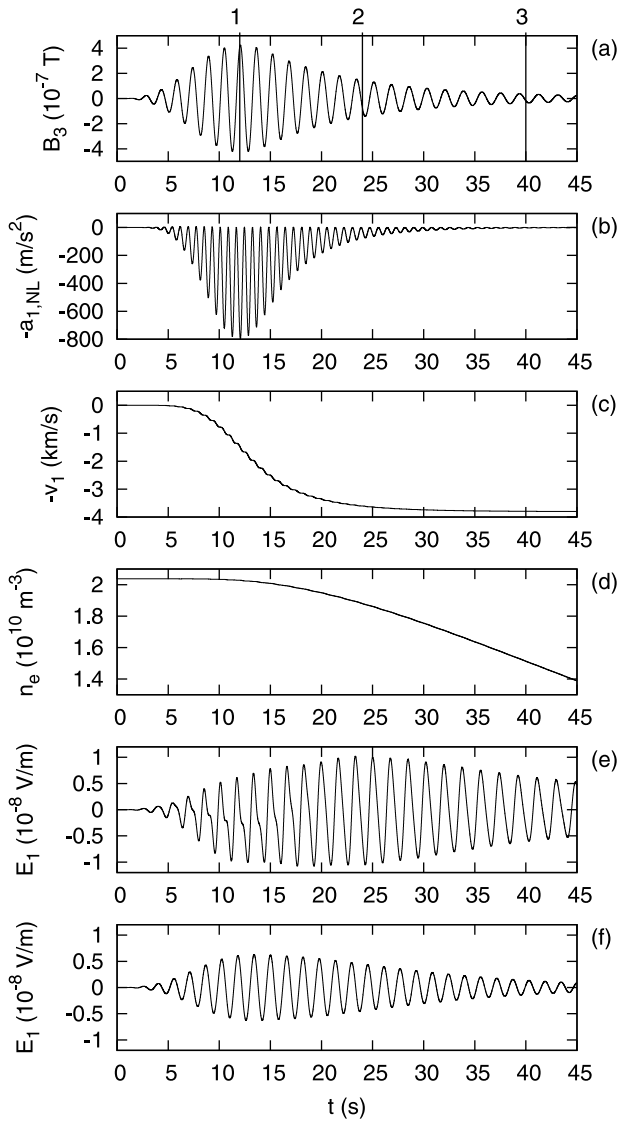


**Figure 8.** Nonlinear simulation with the first IAR harmonic: temporal evolution of the wave magnetic field $B_3$(a), nonlinear force taken with the "minus" sign (b), ion velocity along the geomagnetic field taken with the "minus" sign (c), electron density (d), wave electric field $E_1$ (e). (f) Temporal evolution of the wave electric field $E_1$ in a linear simulation with the same initial and incoming wave parameters as the nonlinear simulation above. All dependences are obtained at a point located on the middle field line at a distance of $L_1$ = 652 km from the ionospheric boundary. Negative values in (b) and (c) are directed downward, towards the ionospheric boundary $L_1$ = 0. Vertical lines 1, 2, and 3 in (a) mark times $t_1$ = 12 s, $t_2$ = 24 s, and $t_3$ = 40 s, respectively. Profiles in Figure 9 are obtained at these times.

convective nonlinearities in the plasma equations of motion [*Chaston et al.*, 2007], and electron acceleration by stationary Alfvén waves [*Knudsen*, 1996].

[37] It is instructive to investigate how the evolution of IAR oscillations towards smaller transverse wavelength will be reflected in ground-based observations. The intensity of an aurora is proportional to the intensity of electron precipitation. One can consider the electric current created by the downward electron flow at the ionospheric boundary as a proxy of auroral emissions. The temporal evolution of spatial distribution of the upward electric current is shown by the grey-scale map in Figure 10. This figure approximates the expected keogram of the aurora below the excited IAR.

## 6. Discussion of the Model Justification and Validity of the Results

[38] In the 2D IAR model, the effects of plasma pressure, curvature of the geomagnetic field, and gravity force are omitted. These simplifications lead to some limitations of the model. The consequences of omitting the thermal effects in the simulation with the first IAR harmonic are as follows. The contraction of plasma at the converging point $L_1 \approx$ 450 km produces a narrow density spike shown in Figure 7e. The growth of the spike amplitude is not limited in the present model because the plasma is assumed cold. In a plasma with finite temperature, the growth of such a spike will be limited by the pressure gradient. A simple estimate of the threshold plasma temperature follows from the condition that the pressure gradient $k_1 nT$ is equal to the average nonlinear force $\langle env_{O,2} B_3 \rangle$, here $n$ is the plasma density and the contribution of hydrogen ions is omitted because in the IAR $n_O \gg n_H$. Using (20), one obtains

$$T \approx \frac{m_O}{2} \left( \frac{E_2}{B_E} \right)^2 .$$

In this equation, $T$ can be the temperature of electrons or oxygen ions. For $E_2 \approx 0.8$ V/m and $B_E \approx 4.3 \times 10^{-5}$ T near the maximum of the density spike, and $m_O = 2.656 \times 10^{-26}$

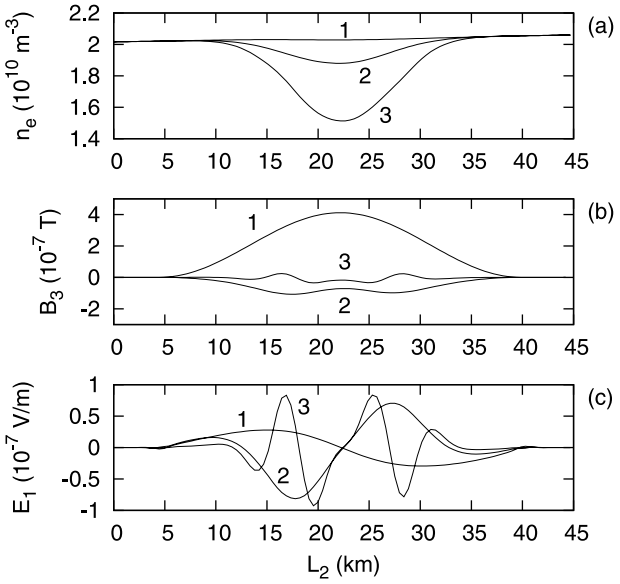


**Figure 9.** Transverse profiles of plasma density (a), wave magnetic field (b), and wave electric field $E_1$ (c). Everywhere, curves 1, 2, and 3 correspond to times $t_{1,2,3}$ marked by vertical lines in Figure 8a, respectively. Profiles are obtained along the line $\xi_1 = const$ which has its midpoint at a distance $L_1$ = 652 km from the ionospheric boundary.

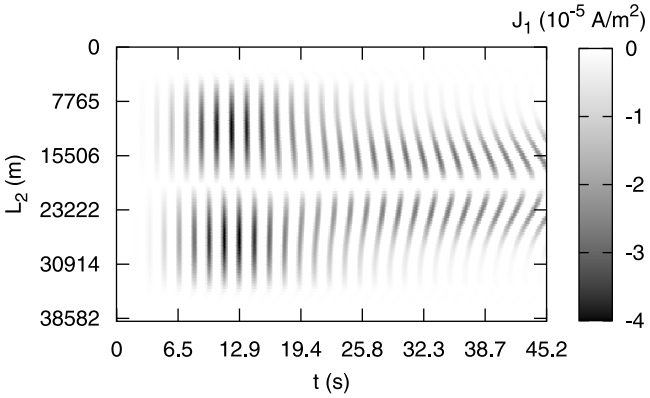


**Figure 10.** Spatial and temporal evolution of the upward directed electric current produced by precipitating electrons at the ionospheric boundary in simulation with the first IAR harmonic. The intensity of the upward current is shown by the gray scale. The vertical axis is the distance from the Northern end of the ionospheric boundary (point $B$ in Figure 3). The horizontal axis is the time.

kg, the critical temperature at which the thermal effects may compensate the density modification due to the nonlinear force of the Alfvén wave is $T \approx 29$ eV. This value is much larger than typical temperatures of plasma components at altitudes below 5000 km, which is about 0.5 eV for ions [*Ergun et al.*, 2000] and 1–5 eV for electrons [*Kletzing et al.*, 1998]. However, plasma pressure is important if the model will be used to follow the evolution of the IAR plasma for longer periods (more than one minute for the present parameters) – test simulations reveal that in this case both the plasma density and its gradient near converging points can become unphysically high without the compensating action of the plasma pressure. Plasma pressure should be considered if the model is extended to include processes at higher altitudes (above 1–2 Earth radii), where the ion and electron populations may have temperatures of the order of a few keV [e.g., *Ergun et al.*, 2000].

[39] The gravity force and the centrifugal force (curvature effect) produce additional acceleration along geomagnetic field. At a point located at a distance $L_1$ from the ionospheric boundary, the gravity force acceleration can be estimated as

$$a_g(L_1) \approx -g \frac{R_E^2}{(R_E + h_I + L_1)^2}, \qquad (22)$$

where $g = 9.8$ m/s$^2$, the negative sign shows that this acceleration is directed downward. The upward directed centrifugal acceleration can be estimated as

$$a_{\alpha,c}(L_1) \approx \frac{\langle v_{\alpha,2}^2 + v_{\alpha,3}^2 \rangle}{R_E + h + L_1}, \alpha = O, H, \qquad (23)$$

where averaging $\langle \ldots \rangle$ is performed over one period of the IAR oscillations. Finally, the estimate of the contribution of the wave electric field $E_1$ is

$$a_{\alpha,E_1}(L_1) \approx \frac{\langle |E_1| \rangle}{e m_\alpha}, \alpha = O, H, \qquad (24)$$

where averaging $\langle \ldots \rangle$ is performed both in time, over one period of the IAR, and in space, over cross sections $\xi_1 = const$. The time averaged absolute values of the accelerations along the geomagnetic field related with different forces [equations (20), (22), (23), and (24)] are compared in Figures 11a and 11b for the simulation with the fundamental and the first IAR harmonic, respectively.

[40] For the fundamental IAR harmonic, the nonlinear force acceleration (bold curve in Figure 11a) is stronger than accelerations due to all other forces for $0 < L_1 < 1700$ km. At higher altitudes, the centrifugal force (dash-dot curve in Figure 11a) is the strongest, while the effect of the wave electric field $E_1$ on hydrogen ions (upper dashed curve in Figure 11a) becomes comparable with the nonlinear force.

[41] The nonlinear force is stronger for the first IAR harmonic because the wavelength of this harmonic is shorter. As a result, the nonlinear force of the first harmonic (bold curve in Figure 11b) is dominant for $0 < L_1 < 2600$ km, i.e., in the most part of the IAR region. At higher altitude, the nonlinear force is comparable to the centrifugal force (dash-dot curve in Figure 11b) and, for hydrogen ions, to the force due to the Alfvén wave electric field $E_1$ (upper dashed curve in Figure 11b).

[42] In both cases, the gravity force acceleration (solid thin curves in Figure 11) and, for oxygen ions, the acceleration due to the wave electric field $E_1$ (lower dashed curves in Figure 11) are much smaller than the nonlinear force acceleration. Note, however, that the nonlinear and the centrifugal forces are proportional to the squared wave

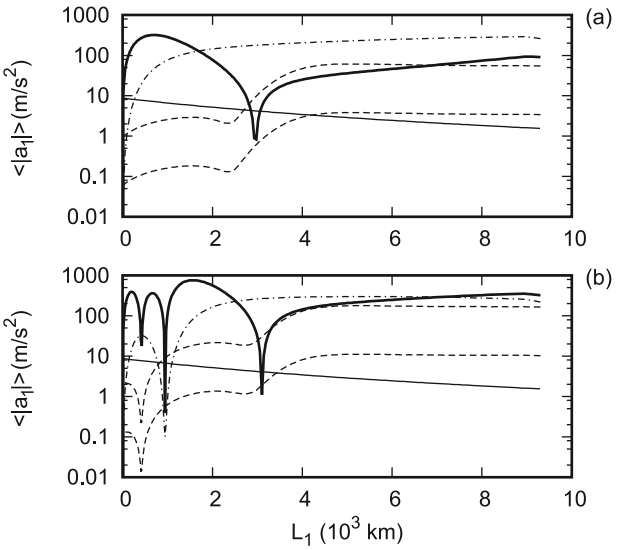


**Figure 11.** Profiles of absolute values of ion accelerations along the geomagnetic field caused by the nonlinear force [bold curve, equation (20)], gravity force [solid thin curve, equation (22)], centrifugal force [dash-dot curve, equation (23)], and wave electric field $E_1$ [dashed curves, equation (24), a higher/lower curve corresponds to hydrogen/oxygen ions]. Figure (a) is for the simulation with the fundamental IAR harmonic, averaging is performed over one wave period starting at $t = 15.8$ s (same as in Figure 6). Figure (b) is for the simulation with the first IAR harmonic, averaging is performed over one wave period starting at $t = 12.5$ s (same as in Figure 7).

amplitude, thus, for low amplitude waves these forces can become comparable to or less than the force of the wave electric field $E_1$ or even the gravity force.

## 7. Conclusion

[43] A two-dimensional multi-fluid MHD model of IAR has been developed. The model describes propagation of a low frequency Alfvén wave in a cold strongly non-uniform near-Earth plasma in the nonlinear regime. Numerical simulations reveal that when the first harmonic of the IAR is excited, the nonlinear Lorentz force (related to the action of the magnetic field of IAR oscillations on the transverse ion current) produces a density depression at altitudes above the ionosphere from 550 km to 1350 km. If the IAR is excited by an Alfvén wave coming from the high-altitude magnetosphere with amplitude of $E_2 = 0.5$ V/m, the density depression reaches about 45% of the ambient density within timescales of a minute or so. The amplitude and the location of the density depression qualitatively agrees with satellite measurements. The intensity of the incoming wave, although high, is still within the measured range.

[44] The profile of the density perturbation, and the related profile of the Alfvén speed across the geomagnetic field follow the profile of the Alfvén wave intensity. As a result, phase mixing of oscillations on neighboring geomagnetic field lines develops and the transverse wavenumber of the oscillations grows. This process is accompanied by amplification of the wave electric field directed along the geomagnetic field.

[45] The model has several simplifications. The gravity force, the terms related with the curvature, and the terms related with thermal effects are omitted. Estimations show that these assumptions are reasonable for the selected regimes of simulation. Inclusion of these effects, as well as those of the mirror force and the finite ionospheric conductivity into the model is left for future work. Note, a feedback instability, which is omitted in the current model, requires changing of the ionospheric conductivity in response to the intensity of the incident Alfvén wave [*Lysak*, 1991]. In case of nonuniform wave intensity, the gradient of the conductivity along the ionospheric boundary may appear, which is another mechanism capable to produce large transverse wavenumbers in the IAR [*Streltsov and Lotko*, 2004].

[46] **Acknowledgments.** The present research was supported by the Natural Sciences and Engineering Research Council of Canada (NSERC) and the Canadian Space Agency (CSA).

[47] Wolfgang Baumjohann thanks Robert Lysak and another reviewer for their assistance in evaluating this paper.

## References

Allan, W. (1993), Plasma energization by the ponderomotive force of magnetospheric standing Alfvén waves, *J. Geophys. Res.*, *98*, 11,383–11,390.

Andre, M., and A. Yau (1997), Theories and observations of ion energization and outflow in the high latitude magnetosphere, *Space Sci. Rev.*, *80*, 27–48.

Bellan, P. M., and K. Stasiewicz (1998), Fine scale cavitation of ionospheric plasma caused by inertial Alfvén wave ponderomotive force, *Phys. Rev. Lett.*, *80*, 3523–3526.

Boehm, M. H., C. W. Carlson, J. P. McFadden, J. H. Clemmons, and F. S. Mozer (1990), High-resolution sounding rocket observations of large-amplitude Alfvén waves, *J. Geophys. Res.*, *95*, 12,157–12,171.

Chaston, C. C., J. W. Bonnell, C. W. Carlson, M. Berthomier, L. M. Peticolas, I. Roth, J. P. McFadden, R. E. Ergun, and R. J. Strangeway (2002), Electron acceleration in the ionospheric Alfvén resonator, *J. Geophys. Res.*, *107*(A11), 1413, doi:10.1029/2002JA009272.

Chaston, C. C., A. J. Hull, J. W. Bonnell, C. W. Carlson, R. E. Ergun, R. J. Strangeway, and J. P. McFadden (2007), Large parallel electric fields, currents, and density cavities in dispersive Alfvén waves above the aurora, *J. Geophys. Res.*, *112*, A05215, doi:10.1029/2006JA012007.

Cummings, W. D., R. J. O'Sullivan, and P. J. Coleman Jr. (1969), Standing Alfvén waves in the magnetosphere, *J. Geophys. Res.*, *74*, 778–793.

Ergun, R. E., C. W. Carlson, J. P. McFadden, F. S. Mozer, and R. J. Strangeway (2000), Parallel electric fields in discrete arc, *Geophys. Res. Lett.*, *27*, 4053–4056.

Eriksson, A. I., B. Holback, P. O. Dovner, R. Bostrom, G. Holmgren, M. Andre, L. Eliasson, and P. M. Kintner (1994), Freja observations of correlated small-scale density depletions and enhanced lower hybrid waves, *Geophys. Res. Lett.*, *21*, 1843–1846.

Feygin, F. Z., O. A. Pokhotelov, D. O. Pokhotelov, T. Braysy, J. Kangas, and K. Mursula (1997), Exo-plasmaspheric refilling due to ponderomotive forces induced by geomagnetic pulsations, *J. Geophys. Res.*, *102*, 4841–4845.

Gaponov, A. V., and M. A. Miller (1958), Potential wells for charged particles in high-frequency electromagnetic field, *Sov. Phys. JETP*, *7*, 168–169.

Genot, V., P. Louarn, and F. Mottez (2000), Electron acceleration by Alfvén waves in density cavities, *J. Geophys. Res.*, *105*, 27,611–27,620.

Genot, V., P. Louarn, and F. Mottez (2004), Alfvén wave interaction with inhomogeneous plasmas: Acceleration and energy cascade towards small-scales, *Ann. Geophys.*, *22*, 2081–2096.

Godyak, V., R. Piejak, B. Alexandrovich, and A. Smolyakov (2001), Observation of the ponderomotive effect in an inductive plasma, *Plasma Sources Sci. Technol.*, *10*, 459–462.

Guglielmi, A., and R. Lundin (2001), Ponderomotive upward acceleration of ions by ion cyclotron and Alfvén waves over the polar regions, *J. Geophys. Res.*, *106*, 13,219–13,236.

Guglielmi, A. V., O. A. Pokhotelov, L. Stenflo, and P. K. Shukla (1993), Modifications of the magnetospheric plasma due to ponderomotive forces, *Astrophys. Space Sci.*, *200*, 91–96.

Heyvaerts, J., and E. R. Priest (1983), Coronal heating by phase-mixed shear Alfvén waves, *Astron. Astrophys.*, *117*, 220–234.

Kentwell, G. W., and D. A. Jones (1987), The time-dependent ponderomotive force, *Phys. Reports*, *145*, 319–403.

Kletzing, C. A., F. S. Mozer, and R. B. Torbert (1998), Electron temperature and density at high latitude, *J. Geophys. Res.*, *103*, 14,837–14,845.

Knudsen, D. J. (1996), Spatial modulation of electron energy and density by nonlinear stationary inertial Alfvén waves, *J. Geophys. Res.*, *101*, 10,761–10,772.

Knudsen, D. J., et al. (2004), Lower-hybrid cavity density depletions as a result of transverse ion acceleration localized on the gyroradius scale, *J. Geophys. Res.*, *109*, A04212, doi:10.1029/2003JA010089.

Krushelnick, K., A. Ting, C. I. Moore, H. R. Burris, E. Esarey, P. Sprangle, and M. Baine (1997), Plasma channel formation and guiding during high intensity short pulse laser plasma experiments, *Phys. Rev. Lett.*, *78*, 4047–4050.

LeVeque, R. J. (1992), *Numerical Methods for Conservation Laws, Lectures in Mathematics*, 2nd ed., pp. 58–59, Birkhauser Verlag, Basel.

Li, X., and M. Temerin (1993), Ponderomotive effects on ion acceleration in the auroral zone, *Geophys. Res. Lett.*, *20*, 13–16.

Lundin, R., L. Eliasson, G. Haerendel, M. Boehm, and B. Holback (1994), Large-scale auroral plasma density cavities observed by Freja, *Geophys. Res. Lett.*, *21*, 1903–1906.

Lysak, R. L. (1991), Feedback instability of the ionospheric resonant cavity, *J. Geophys. Res.*, *96*, 1553–1568.

Lysak, R. L. (2004), Magnetosphere-ionosphere coupling by Alfvén waves at midlatitudes, *J. Geophys. Res.*, *109*, A07201, doi:10.1029/2004JA010454.

Lysak, R. L., and Y. Song (2000), The role of Alfvén waves in the formation of auroral parallel electric fields, in *Magnetospheric Current Systems*, *Geophys. Monogr. Ser.*, vol. 118, edited by S. Ohtani et al., pp. 147–155, AGU, Washington, D. C.

Lysak, R. L., and Y. Song (2005), Nonlocal interactions between electrons and Alfvén waves on auroral field lines, *J. Geophys. Res.*, *110*, A10S06, doi:10.1029/2004JA010803.

Mann, I. R., A. N. Wright, and P. S. Cally (1995), Coupling of magnetospheric cavity modes to field line resonances: A study of resonance widths, *J. Geophys. Res.*, *100*, 19,441–19,456.

Persoon, A. M., D. A. Gurnett, W. K. Peterson, J. J. H. Waite, J. L. Burch, and J. L. Green (1988), Electron density depletions in the nightside auroral zone, *J. Geophys. Res.*, *93*, 1871–1895.

Polyakov, S. V., and C. O. Rapoport (1981), Ionospheric Alfvén resonator, *Geomagn. Aeron.*, *21*, 816.

Rankin, R., P. Frycz, V. T. Tikhonchuk, and J. C. Samson (1994), Nonlinear standing shear Alfvén waves in the Earth's magnetosphere, *J. Geophys. Res.*, *99*, 21,291–21,301.

Rankin, R., J. C. Samson, and V. T. Tikhonchuk (1999), Parallel electric fields in dispersive shear Alfvén waves in the dipolar magnetosphere, *Geophys. Res. Lett.*, *26*, 3601–3604.

Shukla, P. K., L. Stenflo, R. Bingham, and R. O. Dendy (1996), Ponderomotive force acceleration of ions in the auroral region, *J. Geophys. Res.*, *101*, 27,449–27,451.

Singh, N. (1994), Ponderomotive versus mirror force in creation of the filamentary cavities in auroral plasma, *Geophys. Res. Lett.*, *21*, 257–260.

Streltsov, A. V., and W. Lotko (2004), Multiscale electrodynamics of the ionosphere-magnetosphere system, *J. Geophys. Res.*, *109*, A09214, doi:10.1029/2004JA010457.

Trakhtengerts, V. Y., P. P. Belyaev, S. V. Polyakov, A. Demekhova, and T. Boesinger (2000), Excitation of Alfvén waves and vortices in the ionospheric Alfvén resonator by modulated powerful radio waves, *J. Atmos. Solar Terr. Phys.*, *62*, 267–276.

Wahlund, J.-E., and H. J. Opgenoorth (1989), EISCAT observations of strong ion outflows from the F-region ionosphere during auroral activity: Preliminary results, *Geophys. Res. Lett.*, *16*, 727–730.

Watt, C. E. J., R. Rankin, and R. Marchand (2004), Kinetic simulations of electron response to shear Alfvén waves in magnetospheric plasmas, *Phys. Plasmas*, *11*, 1277–1284.

Yeoman, T. K., H. C. Scoffield, D. M. Wright, L. Baddeley, A. N. Vasilyev, and N. V. Semenova (2008), Investigation of natural and artificial stimulation of the ionospheric Alfvén resonator at high latitude, *Adv. Space Res.*, *42*, 957–963.

K. Kabin, R. Rankin, and D. Sydorenko, Department of Physics, University of Alberta, Room 238 CEB, 11322-89 Avenue, Edmonton, AB, Canada T6G 2G7. (kabin@phys.ualberta.ca; rankin@space.ualberta.ca; sydorenk@ualberta.ca)